RESEARCH   **Open Access**

On the modeling and simulation of coupled adsorption and thermosolutal convection in supercritical carbon dioxide

Housseyn Smahi[1,2*], Djilali Ameur[1,2], Joanna Dib[2,3] and Isabelle Raspo[4]

* Correspondence:
smahihousseyne@gmail.com
[1]Laboratory of Theoretical Physics,
University of Abou Bekr Belkaid,
Tlemcen, Algeria
[2]Department of Physics, Faculty of
Sciences, University of Abou Bekr
Belkaid, Tlemcen, Algeria
Full list of author information is
available at the end of the article

Abstract

In this paper, we present a numerical study along with an exhaustive adsorption investigation in a binary dilute mixture model nearby the solvent's critical point in a configuration relevant for soil remediation. By means of this model, mass and heat transfer efficiency were qualitatively and quantitatively discussed through this work. The convergence of the solution was evaluated on the values of the Nusselt and Sherwood numbers. The results reveal intense convection expanding into the cavity close to the critical point, thus enabling homogeneous adsorption of the solute. Moreover, the mass fraction perturbation isolines exhibit the existence, along the adsorbent plate, of a thin boundary layer which becomes thinner when approaching the critical point.

Keywords: Adsorption, Mass transfer, Supercritical carbon dioxide, Mixture fluid, Piston effect, Supercritical fluid deposition

Introduction

Supercritical fluid (SCF) stands for a fluid for which temperature and pressure are set above its gas-liquid critical point. In the supercritical state of matter, the fluid physical properties are intermediate between those of a liquid and a gas, making it a very good solvent. Moreover, SCF are very sensitive to temperature and pressure variations, thus a small change in pressure results in large variations of the fluid density as well as the solubility of solutes. More precisely, in the vicinity of the critical point, these tunable solvents exhibit better mass transfer properties compared to those of liquid solvents due to their higher diffusion coefficient and lower viscosity.

SCF potential applications have known an increasing involvement and significant progress in a wide range of industrial technologies, for instance in various pharmaceutics sectors related to natural substances extraction of biological interest [1–3], agro-food fields [4–7], energy [8], and waste treatment sectors [9–14]. Supercritical carbon dioxide (scCO$_2$) significance has grown fairly quickly in the past decades. It has been extensively investigated in most SCF deposition (SFD) or crystal growth processes and

has been the subject of several researches and publications [15–19]. In fact, SFD is a rising technique for the purpose of depositing metals and metaloxides on surfaces, and is notably relevant for technological processes aiming to prepare supported metallic nanoparticles or metallic films [16, 17]. Moreover, SFD peculiarly employing $scCO_2$ is attractive since carbon dioxide offers many advantages by reason of economic and environmental concerns; it is non-flammable, non-toxic, mainly inexpensive, and remains an attractive solvent since CO_2 critical temperature is near ambient temperature. Additionally, $scCO_2$ has been employed in most of the depositions because no liquid waste is generated, no solvent residue is left on the substrate and the mass transfer rates are fast compared to those of liquids [17]. In addition, the rate and the velocity of the substrate deposition can be controlled by changing the pressure and temperature of the supercritical solvent.

Furthermore, SCF displays very interesting qualities in several potential processes including SCF extraction (SFE) for soil remediation associated with adsorption on activated carbon [20]. This modus operandi was primarily suitable for high molecular weight hydrocarbons [21]. Actually, numerous organics extraction such as that of hexachlorobenzene, phenol, and naphthalene from soil employing $scCO_2$ was reported in [21–24]. However, due to environmental legislation, low contaminant concentration is compulsory. Therefore, an almost contaminant-free process is required when the supercritical solvent is recirculated. As, for volatile pollutants, the solvent and solute disjunction by means of decompression remains inefficacious to attain the requested low concentration criterion, an adsorption supplemental step onto activated carbon remains necessary. In this context, Madras et al. [24] proposed a process coupling supercritical extraction and adsorption for the remediation of soils contaminated by heavy molecular weight organic compounds. In fact, organic pollutants are constantly extracted through $scCO_2$ before being adsorbed on activated carbon. It was established that if the soil desorption is implemented at low temperature, then the process operates in optimum mode if desorption is followed by adsorption at high temperature [24].

Although the widest application of $scCO_2$ is in extraction, the adsorption process using $scCO_2$ exhibits currently more attention and presents a number of potential applications. In fact, several studies investigated the various supercritical adsorption singularities of many systems [12–14, 25–35], thus allowing a selective transfer of species from fluid phase to a solid adsorbent. Moreover, Jha and Madras [31] showed that the heat of adsorption does not depend on the solute considered. When an adsorbent is exposed to a fluid phase, the molecules of the fluid diffuse on its surface. Isothermal adsorption of a particular system provides a source of information on adsorbent pore properties and surface characteristics. The reversible type isotherm is obtained when the adsorption is limited to a few molecular layers. This condition is usually substantiated for adsorption on microporous materials endowed with small-scale external surfaces such as activated carbons. However, SCF adsorption on surfaces or porous particle inner surfaces is much more complex. In fact, in a very close neighborhood of the critical point, the adsorption equilibrium constant is extremely sensitive to temperature and pressure changes leading, especially, to a decrease of the excess amount adsorbed when pressure is increased [32].

In order to devise an adsorption plant, reliable mass transfer models are still necessary. Notwithstanding, exiguous tryouts have been implemented in order to model the

complete supercritical adsorption process, including hydrodynamics [31–35]. That is the reason why this paper aims to investigate adsorption and mass transfer in a binary mixture nearby the solvent's critical point in a configuration relevant for soil remediation. In order to take advantage of the SCF accurate properties and enhance thermodynamics conditions enabling a meliorate adsorption along with a good mass transfer, the influence of critical point vicinity is investigated using numerical simulations in the present work.

Methods

The physical model consists of a dilute mixture of naphthalene (the minority species) and supercritical CO_2, confined in a rectangular cavity of aspect ratio $L/H = 10$ with a heated and adsorbent plate on a part of the bottom boundary as shown in Fig. 1. Naphthalene is the species adsorbed on the bottom plate. It was selected as a model solute because of the wide experimental data of its solubility in $scCO_2$ available in the literature, allowing an easier validation of the thermodynamic model [15]. Moreover, the naphthalene–CO_2 mixture can be considered as a reference system, representative of binary mixtures of interest for SFE and adsorption. The phase diagram of this kind of mixture reveals a discontinuous mixture critical line (Fig. 2). The low-temperature part ceases at the LCEP (lower critical endpoint) that matches with the junction between the solid–liquid–vapor coexistence line and the mixture critical line beginning at the critical point of the solvent (here CO_2). The LCEP is usually slightly above the solvent's critical point. In the same way, the high-temperature part starts at the critical point of the solute (naphthalene) and ends at the UCEP (upper critical endpoint). For temperatures ranging between T_{LCEP} and T_{UCEP}, the mixture exhibits equilibrium between a
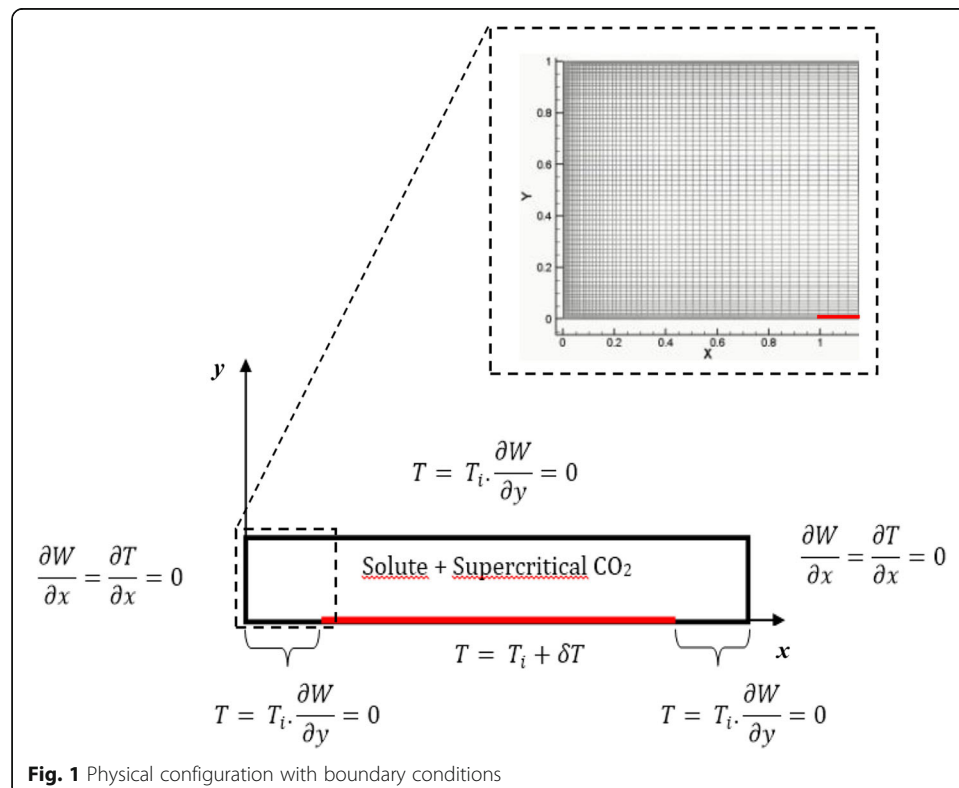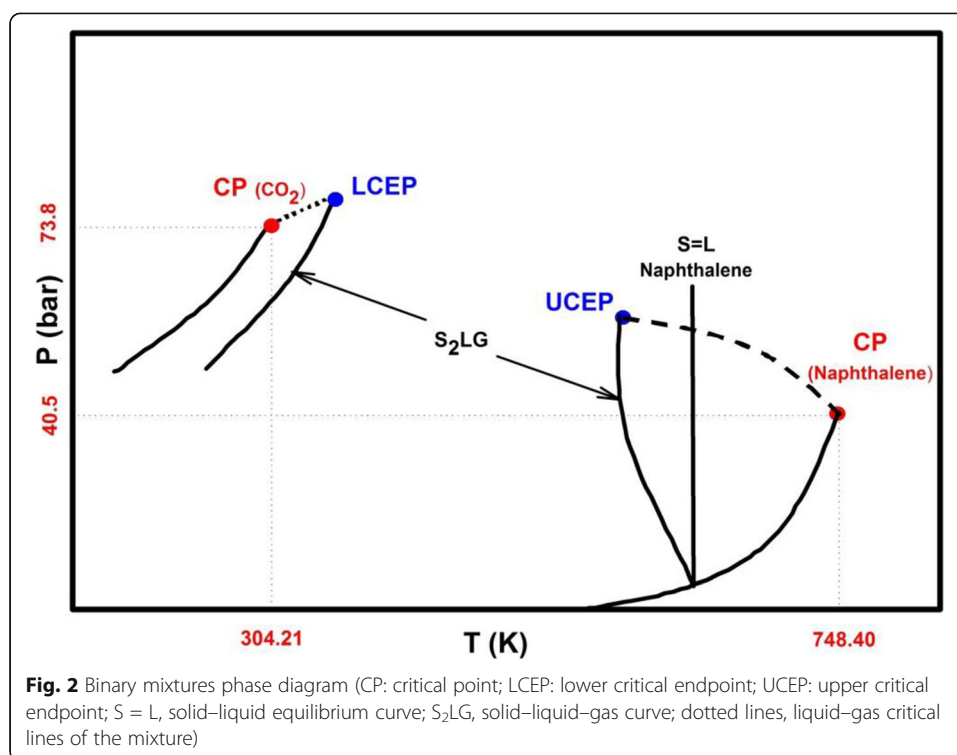

Fig. 1 Physical configuration with boundary conditions

Fig. 2 Binary mixtures phase diagram (CP: critical point; LCEP: lower critical endpoint; UCEP: upper critical endpoint; S = L, solid–liquid equilibrium curve; S₂LG, solid–liquid–gas curve; dotted lines, liquid–gas critical lines of the mixture)

solute solid phase and a mixture fluid phase. In the vicinity of the LCEP, solid solubility and adsorption equilibrium constants are highly sensitive to temperature and pressure variations [15, 32], which points out the reason why SFE and adsorption processes are customarily carried out in the aforementioned phase diagram region. Moreover, near the gas–liquid critical point of a pure compound, fast thermal equilibration is achieved by a thermoacoustic effect, named the piston effect, while thermal diffusion becomes extremely slow [36–38]. More precisely, when the fluid is locally heated, a very thin thermal boundary layer forms along the heated boundary because of the vanishing thermal diffusivity. Since the thermal expansion coefficient diverges near the critical point, this boundary layer strongly expands and adiabatically compresses the bulk fluid leading to a fast and homogenous increase of pressure and bulk temperature. The same phenomenon occurs in mixtures near the solvent's critical point and it was shown in [15, 32] that the strong pressure increase induced by the piston effect has important consequences on the solubility of solids and on adsorption equilibrium constants near the LCEP.

The critical properties of naphthalene and CO_2 together with those of the mixture at the LCEP are reported in Table 1. Initially, at $t = 0$, the fluid is assumed in thermodynamic equilibrium at a uniform temperature T_i slightly higher than the temperature

Table 1 Critical parameters, acentric factor ω, and molar mass M for the pure compounds and the mixture

Component	T_c (K)	ρ_c (kg m^{-3})	P_c (bar)	ω	M (kg mol^{-1})
CO_2	304.21	467.8	73.8	0.225	4.401×10^{-2}
Naphthalene	748.40	314.9	40.5	0.302	1.282×10^{-1}
Naphthalene + CO_2 (LCEP)	307.65	470.0	–	–	–

of the peculiar mixture critical point LCEP, T_{cm} = 307.65 K. Thus, T_i is written as T_i= $(1 + \varepsilon)T_{cm}$, where the parameter $\varepsilon = (T_i - T_{cm})/T_{cm}$ defines the dimensionless proximity to the mixture critical point. The mixture is saturated, i.e., the initial mass fraction w_i corresponds to the solubility of naphthalene in scCO$_2$ at temperature T_i. Additionally, the fluid is stratified along with a mean density equal to the mixture critical density ρ_{cm} = 470 kg m^{-3}. Since ρ_{cm} is very close to the CO$_2$ critical density, the very strong variations of thermophysical properties of CO$_2$ on the critical isochore are still observed.

Weak heating of the order of a few mK per second is then progressively applied at the solid bottom plate corresponding to y = 0 and for x extending between 1 and L/H − 1 (see Fig. 1). In order to avoid discontinuities between isothermal and heated parts of the bottom boundary, the following hyperbolic tangent function is used:

$$\phi(x) = \left[\frac{\tanh(2x{-}4) - \tanh(-4)}{\tanh(2L/H{-}4) - \tanh(-4)} \right] \times \left[\frac{\tanh(2L/H{-}2x{-}4) - \tanh(-4)}{\tanh(2L/H{-}4) - \tanh(-4)} \right] \tag{1}$$

Thus, for ΔT fixed equal to 10 mK for all the simulations, the bottom plate temperature is gradually raised according to the formula:

$$\delta T(t) = \begin{cases} 0.5^\Delta T \left[1 - \cos\left(\pi \dfrac{t}{t_{heat}} \right) \right] \phi(x) & \text{if } t \le t_{heat} \\ {}^\Delta T \phi(x) & \text{if } t > t_{heat} \end{cases} \tag{2}$$

We consider for the mathematical model the 2D compressible time-dependent Navier–Stokes equations, along with the energy and mass diffusion equations together with the Peng–Robinson equation of state. The Peng–Robinson equation implicitly accounts for the divergence of the thermal expansion coefficient β, of the isothermal compressibility χ, and of the specific heat at constant pressure C_P near the liquid-gas critical point of CO$_2$. Carbon dioxide and naphthalene are respectively named components 1 and 2. The governing equations are solved in the low Mach number approximation framework [39] allowing computational cost lessening while accounting for density variations due to compressible effects. In this context, the pressure P is split into two parts: a homogeneous time-dependent thermodynamic part $P_{th}(t)$ looming up in the state and energy equations, and a non-homogeneous dynamic part $P_{dyn}(x, y, t)$ appearing in the momentum equations and depending on time and space. We employed the low Mach number approximation amendment proposed by Accary et al [40] near the critical point in order to account for the strong fluid stratification.

Moreover, we designate by T_{cm}, ρ_{cm}, and H respectively the characteristics temperature, density, and length. Additionally, we consider the piston effect time scale [41] $t_{PE} = t_d/(\gamma - 1)^2$ as being the characteristic time, where t_d and γ are respectively the characteristic time of thermal diffusion and the mixture specific heat ratio (computed from the equation of state [15]), while the corresponding velocity $V_{PE} = H/t_{PE}$ denotes the characteristic velocity.

Since we are dealing with dilute mixtures with CO$_2$ as the majority component, the transport properties such as the dynamic viscosity μ, the specific heat at constant volume C_V, and the thermal conductivity λ, are assumed to be equal to those of pure CO$_2$. As the wall heating considered in this study is small and the divergence of C_V and μ near the critical point is weak, these two properties are supposed to be constant

throughout the simulation and equal to their value for the initial condition. The values provided by the NIST are then used. On the other hand, the correlation of Arai et al. [42] is used for the variation of pure CO_2 thermal conductivity λ. The binary mass diffusion coefficient D_{21} is modeled with the Wilke–Chang equation [43]. All the transport properties are made dimensionless relatively to their initial value.

Thus, the dimensionless governing equations are written:

$$\frac{\partial \rho}{\partial t} + \nabla.(\rho V) = 0 \tag{3}$$

$$\rho \frac{\partial V}{\partial t} + \rho V.\nabla V = -\nabla P_{dyn} + \frac{1}{Re}\Delta V + \frac{1}{3\,Re}\nabla(\nabla.V) - \frac{1}{Fr}(\rho - \rho_i)e_y \tag{4}$$

$$\rho \frac{\partial T}{\partial T} + \rho V.\Delta T = -\frac{C_{VO}}{C_{Vi}}(\gamma_0-1)T\left(\frac{\partial P_{th}}{\partial T}\right)_{\rho,w}(\nabla.V) + \frac{\gamma}{RePr}\nabla.(\lambda^*\nabla T) + \frac{1}{(\gamma-1)^2 Le}\nabla.$$

$$\left[\left((\overline{U_2^*}-\overline{U_1^*}) + \frac{C_{VO}}{C_{Vi}}(\gamma_0-1)P_{th}(\overline{V_2^*}-\overline{V_1^*})\right)\rho D_{21}^*\nabla W\right] - \frac{1}{(\gamma-1)^2 Le}\left[(\overline{U_2^*}-\overline{U_1^*}) + \frac{C_{VO}}{C_{Vi}}(\gamma_0-1)\left(P_{th}-T\left(\frac{\partial P_{th}}{\partial T}\right)_{\rho,W}\right)(\overline{V_2^*}-\overline{V_1^*})\right]\nabla.(\rho D_{21}^*\nabla W) \tag{5}$$

$$\rho \frac{\partial}{\partial} + \rho V.\nabla w = \frac{1}{(\gamma-1)^2 Le}\nabla.\left(\rho D_{21}^*\nabla w\right) \tag{6}$$

where V denotes the velocity of components u and v respectively in the x and y directions, e_y is the unity vector of the Cartesian orthonormal basis, w is the naphthalene mass fraction, γ_0 and C_{v0} denote the corresponding values for a perfect gas (γ_0 = 1.3, $C_{v0} = 3R/M_1$), and λ^* and D_{21}^* correspond respectively to the dimensionless conductivity and mass diffusion coefficient.

In the above equations, the dimensionless parameters stand for the Reynolds number Re, the Froude number Fr, the Prandtl number Pr, and the Lewis number Le respectively defined by:

$$Re = \frac{\rho_{cm}V_{PE}H}{\mu_i}, \quad Fr = \frac{V_{PE}^2}{gH}, \quad Pr = \frac{\mu_i\gamma C_{Vi}}{\lambda_i} \quad \text{and} \quad Le = \frac{\lambda_i}{\rho_{cm}\gamma C_{Vi}(D_{21})_i}$$

Two other dimensionless parameters are of interest for the present problem: the Mach and the Rayleigh numbers respectively defined by:

$$Ma = \frac{V_{PE}}{C_O} \quad \text{and} \quad Ra = \frac{\rho_{cm}^2\gamma C_{Vi}g\beta i\Delta TH^3}{\mu_i\lambda_i}$$

where $c_0 = \sqrt{\gamma_0(\frac{R}{M_1})T_{cm}}$ denotes the sound speed with R = 8.3145 J mol^{-1} K^{-1} the perfect gas constant. In Eq. (5), $\overline{U_k^*}$ and $\overline{V_k^*}$ denote respectively the dimensionless partial molar internal energy and volume expressed as follows:

$\overline{U_k^*} = \overline{U_k}/(M_2 C_{Vi}T_{cm})$ and $\overline{V_k^*} = \overline{V_k}/(M_2/\rho_{cm})$ for k = 1, 2

where $\overline{U_k}$ and $\overline{V_k}$ represent respectively the partial molar internal energy and volume, computed from the Peng–Robinson equation [15].

The mixture thermodynamic state is described by the Peng–Robinson equation of state in the framework of the one-fluid theory:

$$P_{th} = \frac{T\rho\theta(w)}{1 - \frac{b*(w)\rho}{\theta(w)}} - \frac{a*(T,w)\rho^2}{1 + 2b*(w)\rho/\theta(w)^2\rho^2/\theta(w)^2} \tag{7}$$

where $\theta(w) = 1 - (1 - \frac{M_1}{M_2})w$, $a^*(T,w) = a^*_1(T)(1-w)^2 + 2a^*_{12}(T)w(1-w) + a^*_2(T)w^2$

and $b^*(w) = b^*_1(1-w)^2 + 2b^*_{12}w(1-w) + b^*_2w^2$

with

$$a^*_1(T) = 1.487422\frac{T_{c1}}{T_{cm}}\frac{\rho_{cm}}{\rho_{c1}}\left[1 + \beta_1\left(1 - \sqrt{T(T_{cm}/T_{c1})}\right)\right]^2,$$

$$a^*_2(T) = 1.487422\frac{M_1}{M_2}\frac{T_{c2}}{T_{cm}}\frac{\rho_{cm}}{\rho_{c2}}\left[1 + \beta_2\left(1 - \sqrt{T(T_{cm}/T_{c2})}\right)\right]^2,$$

$$a^*_{12}(T) = \sqrt{a^*_1(T)a^*_2(T)}(1-k_{12}), \quad b^*_j = 0.253076\left(\frac{\rho_i}{\rho_{cj}}\right) \text{ for } j = (1,2),$$

$$b^*_{12} = \frac{1}{2}\left(b^*_1\frac{M_1}{M_2} + b^*_2\right)(12l_{12}) \text{ and } \beta_j = 0.37464 + 1.54226\omega_j - 0.26992\omega_j^2 \text{ for } j = (1,2),$$

where ω is the acentric factor (see Table 1) and the superscript (*) refers to dimensionless quantities. The binary interaction parameters k_{12} and l_{12} were fitted on experimental solubility data and depend on initial temperature as [15]:

$k_{12} = 0.0395 + 0.0114(\frac{308.15}{T_i} - 1)$ and $l_{12} = -0.1136 - 0.3103(\frac{308.15}{T_i} - 1)$

On the adsorbent plate, the adsorption reaction is modeled by a first-order reaction. As for temperature, the discontinuity between the non-reactive parts and the adsorbent plate is prevented by the use of the function Φ (Eq. (1)). The boundary condition for w on the bottom wall is then:

$$D_{21}\frac{\partial w}{\partial y} = -K_a w\Phi(x) \tag{8}$$

where K_a is the adsorption constant depending on temperature and pressure. In view of small temperature differences ΔT considered, K_a is linearized as follows [32]:

$$K_a = K_{ai} + \left(\frac{\partial K_a}{\partial T}\right)_P (T - T_i) + \left(\frac{\partial K_a}{\partial P}\right)_T (P_{th} - P_{thi}) \tag{9}$$

The derivatives $(\partial K_a/\partial T)_P$ and $(\partial K_a/\partial P)_T$ depend on those of the adsorption equilibrium constant that diverge near the solvent's critical point [32]. It is notable that this divergent behavior is not specific to naphthalene but it is a universal behavior for dilute mixtures since it is due, in particular, to the divergence of the solute infinite dilution partial molar volume [44]. In dimensionless form, the boundary condition (8) is written as:

$$\frac{\partial w}{\partial y} = -\left(\frac{DaD_k}{D^*_{21}}\right)w\Phi(x)$$

with Da = $HK_{ai}/(D_{21})_i$ the Damköhler number and

$$D_k = 1 + \frac{1}{K_{ai}} \left(\frac{\partial K_a}{\partial T} \right)_p (T - T_i) + \frac{1}{K_{ai}} \left(\frac{\partial K_a}{\partial P} \right)_T (P_{th} - P_{thi})$$

The mathematical model is completed by the following boundary conditions (Fig. 1):

- No-slip conditions are prescribed for velocity on all the boundaries;

- A homogeneous Neumann boundary condition is applied for w at the non-reactive vertical and upper walls;

- The vertical walls are adiabatic while the horizontal ones are kept at the initial temperature, except for the heated plate where a Dirichlet boundary condition is used for T:

$$T = T_i + \delta(t) \text{ with } \delta(t) \text{ define by Eq.2} \tag{10}$$

The code employed in this study is homemade [32–34]. The numerical method is based on a second-order semi-implicit scheme for time discretization and a spectral collocation method for space approximation to ensure a high accuracy (see [12]). The Gauss Lobatto collocation points are used. The mesh is therefore naturally refined near the walls, allowing a better representation of the thin thermal boundary layers. The refined mesh size near the walls is in the order of 3×10^{-4} mm (about 20% of grid points inside the boundary layers). The convergence of the solution in terms of mesh size was evaluated on the values of the Nusselt and Sherwood numbers. It was found that a mesh 251×81 was sufficient.

Results and discussion

In the present work, numerical simulations were carried out for three initial temperatures T_i = 308.15 K, 309.15 K, and 318.15 K. These various temperatures correspond to distances to the mixture critical point equal to 0.5 K, 1.5 K, and 10.5 K respectively. The initial mass fraction w_i dovetails with the solubility of naphthalene in CO_2, which means that the mixture is saturated. The transport properties values obtained for these initial conditions are reported in Table 2.

While the critical temperature is nearing, we perceive the strong increase of the thermal expansion coefficient β, the thermal conductivity λ along with the specific heat ratio γ. These behaviors lead to the strong Rayleigh, Reynolds, Froude, and Prandtl numbers increment as T_i is decreased from 318.15 to 308.15 K (see Table 3). Moreover, it must be highlighted that the Damköhler number Da was set at 10^{-5} for all the simulations, which is a relevant value for adsorption of Naphthalene. Indeed, from available literature data [12–14, 30], the Damköhler number for adsorption of naphthalene on various solids can be estimated in the range 10^{-14}–10^{-3}. However, it was shown in [32] that the phenomena observed for the adsorption reaction near the LCEP are qualitatively the same whatever the value of Da. The Damköhler number measures the relative

Table 2 Transport coefficients corresponding to various temperature values T_i

T_i (K)	μ_i (Pa s)	λ_i (W m K^{-1})	C_{Vi} (J kg K^{-1})	$(D_{21})_i$ (m^2 s^{-1})	β_i (K^{-1})
308.15	3.3402×10^{-5}	9.6172×10^{-2}	1306.27	2.1969×10^{-8}	2.3134×10^{-1}
309.15	3.3448×10^{-5}	9.1322×10^{-2}	1269.32	2.2009×10^{-8}	1.7465×10^{-1}
318.15	3.3870×10^{-5}	6.6804×10^{-2}	1074.57	2.2368×10^{-8}	5.4955×10^{-2}

Table 3 Values of the dimensionless parameters for the three initial temperatures

T_i (K)	ε	Re	Le	Ma	Fr	Ra	Pr
308.15	1.6252×10^{-3}	59.46	0.43	1.54×10^{-5}	1.82×10^{-3}	34138.57	7.59
309.15	4.8756×10^{-3}	41.09	0.49	1.06×10^{-5}	8.72×10^{-4}	21638.09	6.49
318.15	3.4129×10^{-2}	9.97	0.90	2.61×10^{-6}	5.26×10^{-5}	3490.59	3.55

importance of adsorption rate compared to diffusion rate. Therefore, when Da $\ll$ 1, mass diffusion is much faster than adsorption so that it reaches equilibrium before adsorption.

Stability and convergence to the steady state

The values of different characteristic times for each simulation case are listed in Table 4. We can note the strong increase of the thermal diffusion characteristic time and the strong decrease of the piston effect time scale as the critical temperature is approached. On the other hand, the mass diffusion characteristic time does not change very much with temperature.

The solution state (stationary, periodic, chaotic) is evaluated on the temporal evolution of the temperature perturbation $T - T_i$ at $x = L/2$ and in the hot boundary layer (Fig. 3a) and in the middle of the cavity (Fig. 3b) for the three initial temperatures. Qualitatively, the different curves of Fig. 3 indicate that a stationary solution is obtained. The temperature in the hot boundary layer stabilizes faster for the three initial conditions (around $t = 60$ s). In the middle of the cavity, the stabilization time increases as the initial temperature decreases to the critical point value (Fig. 3b): around 62 s, 92 s, and 99 s for $T_i = 318.15$ K, 309.15 K, and 308.15 K, respectively. These values are globally consistent with the thermal diffusion characteristic times reported in Table 4. Obviously, convection also influences the temperature homogenization inside the cavity and Table 3 shows that the Rayleigh number strongly increases when T_i is closer to the critical temperature. Therefore, convection is much more intense at $T_i = 308.15$ K than at $T_i = 318.15$ K, as discussed in section 5.2. Figure 4 presents the vertical profiles of temperature at $x = L/2$ for different times and for the three initial conditions. A completely different behavior is observed far and close to the mixture critical point. For $T_i = 318.15$ K, a diffusive profile is almost achieved at $t = 6$ s and the final increase of the bulk temperature is then induced by convection. For the two smaller initial temperatures, the final temperature profile still exhibits a boundary layer-like variation. Moreover, the temperature profiles reveal that a time larger than 100 s is required to reach convergence. That is the reason why, for the rest of this paper, all the results are represented at a time greater than this reference convergence time.

Table 4 Piston effect, t_{PE}, thermal diffusion, t_d, and mass diffusion, t_{md}, characteristic times for the three initial temperatures

T_i (K)	t_{PE} (s)	t_d (s)	t_{md} (s)
308.15	0.2366	106.9022	45.5194
309.15	0.3419	91.1253	45.4358
318.15	1.3916	49.2332	44.7069

Fig. 3 Temporal evolution of temperature in the hot boundary layer **(a)** and at mid-height **(b)** for the three initial temperatures 308.15 K, 309.15 K, and 318.15 K
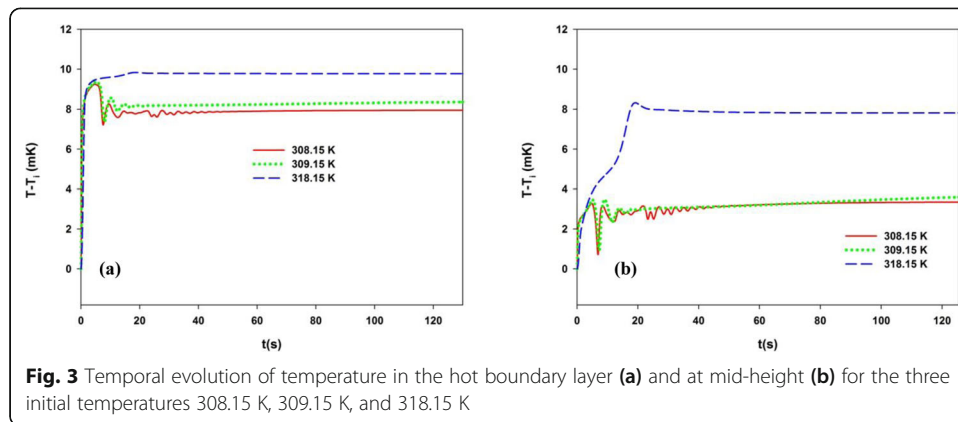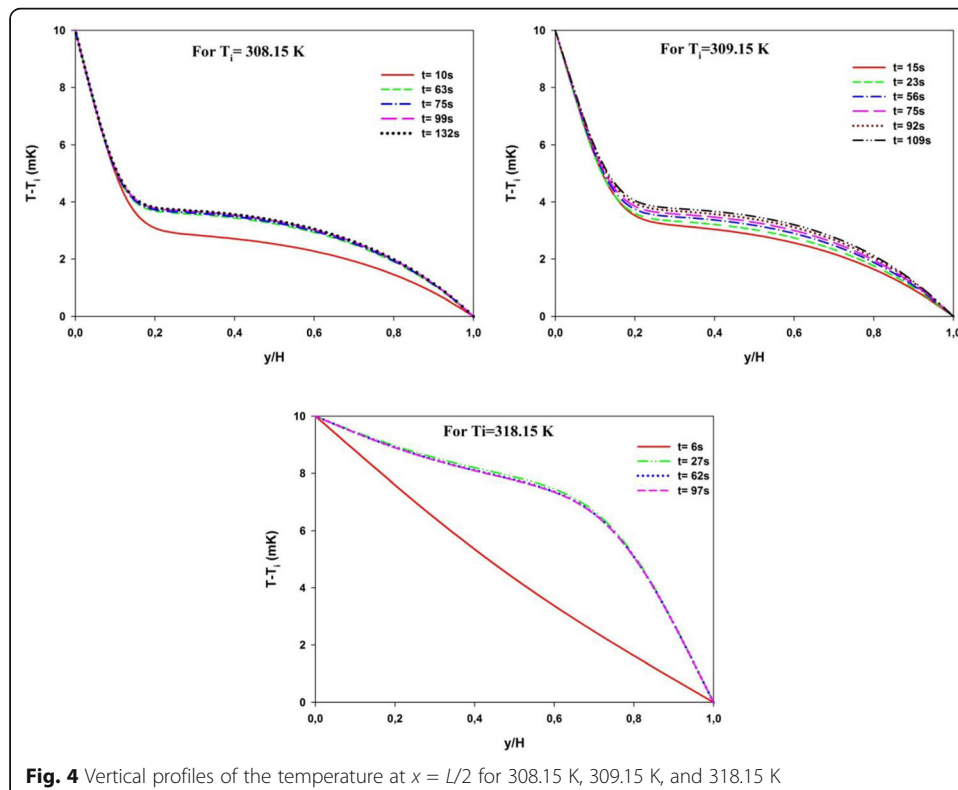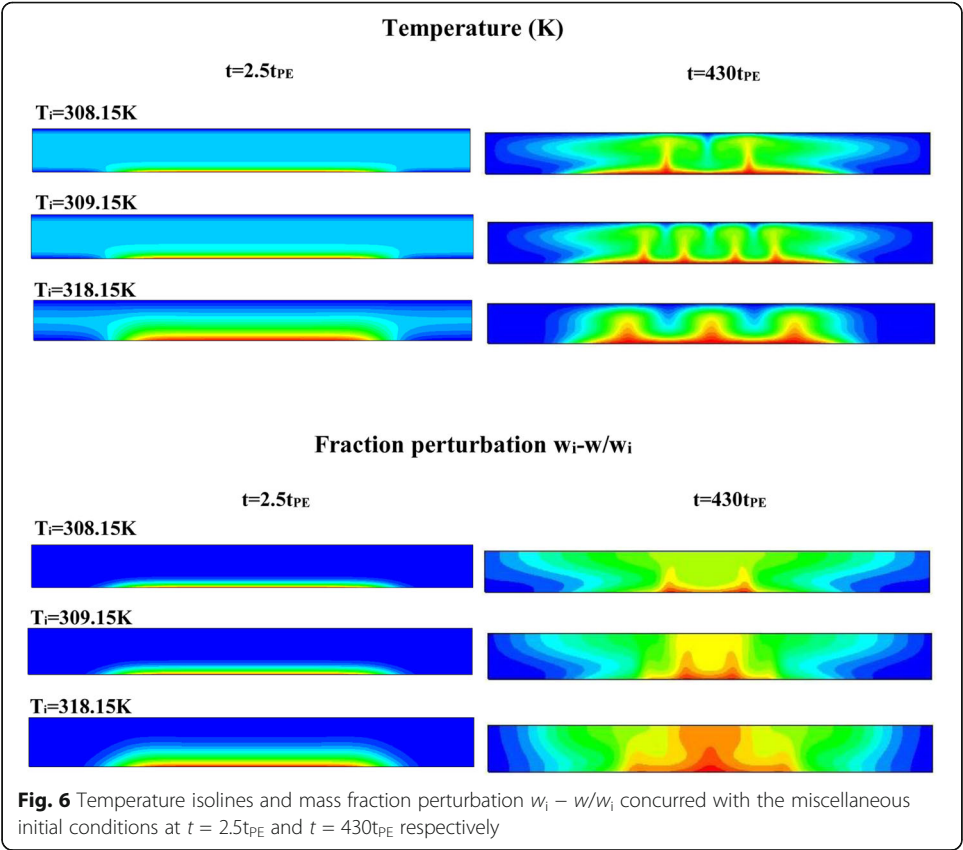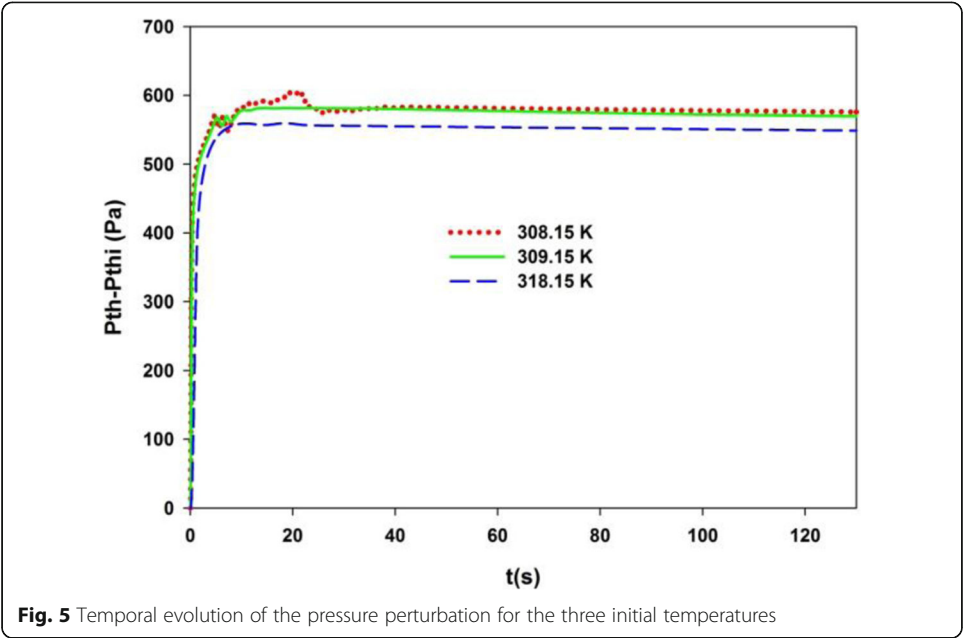
Figure 5 shows the temporal evolution of the thermodynamic pressure for the three initial temperatures. In all the cases, we observe the strong pressure increase, typical of the piston effect, from the beginning of the simulation. We note also that the pressure level that reached convergence is higher as the critical temperature is approached, corresponding to the divergence of isothermal compressibility near the critical point. This larger pressure increase obviously has an effect on the adsorption as shown by Eq. (9).

Heat and mass transfer investigation in the vicinity of the lower critical endpoint

We are interested in the following section on the effect of the vicinity to the mixture critical point on temperature and mass fraction fields inside the cavity. Figure 6 displays

Fig. 4 Vertical profiles of the temperature at $x = L/2$ for 308.15 K, 309.15 K, and 318.15 K

Fig. 5 Temporal evolution of the pressure perturbation for the three initial temperatures

Fig. 6 Temperature isolines and mass fraction perturbation $w_i - w/w_i$ concurred with the miscellaneous initial conditions at $t = 2.5t_{PE}$ and $t = 430t_{PE}$ respectively
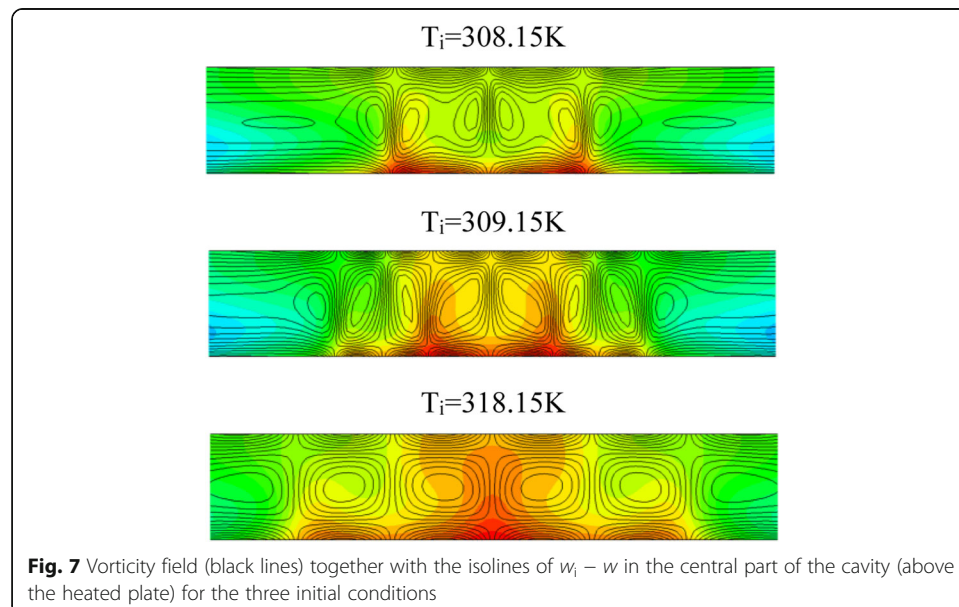
the temperature isolines and mass fraction perturbation at two different times corresponding to $2.5t_{PE}$ and $430t_{PE}$ for the three initial conditions. The solutions obtained for the various values of T_i are similar. The temperature field at this time is governed by the piston effect, as in pure CO_2 [41], with three distinct zones: a hot boundary layer along the heated plate, cold boundary layers along isothermal walls, and the cavity bulk that is homogeneously heated by the piston effect. In addition, as in pure CO_2, the thermal boundary layers are thinner when approaching the critical point because of the strong decrease of thermal diffusivity. In the same way, since Da $\ll$ 1, the mass fraction near the adsorbent plate is governed by mass diffusion. Indeed, the isolines of the mass fraction perturbation reveal the existence, along the adsorbent plate, of a thin boundary layer that becomes thinner when approaching the critical point because of the decrease of the mass diffusion coefficient D_{21} (Table 2). Figure 6 also presents the steady solution obtained for each initial condition. Concerning the mass fraction, it must be underlined that, although the isoline map does not evolve anymore, the values of $w_i - w$ keeps on increasing while the adsorption reaction still goes on. Indeed, since Da $\ll$ 1, the reaction will reach equilibrium much later than mass diffusion.

As expected, the temperature field is very different depending on the proximity to the critical point. Because of the diverging behavior of the thermal expansion coefficient β (Table 2), the Rayleigh number strongly increases as approaching the critical temperature (Table 3): Ra = 3683 for T_i = 318.15 K, Ra = 21938 for T_i = 309.15 K, and Ra = 34139 for T_i = 308.15 K. Consequently, the convective flow is much more intense for T_i = 308.15 K (Fig. 6), allowing a better mixing inside the cavity. We have calculated the flow enstrophy defined by:

$$E = \int \int |\nabla \times V|^2 dxdy$$

This physical quantity, directly related to the norm of the vorticity $\nabla \times V$, is a kind of measure of the vortices intensity inside the cavity. It was found that E strongly

Fig. 7 Vorticity field (black lines) together with the isolines of $w_i - w$ in the central part of the cavity (above the heated plate) for the three initial conditions

increases as the critical point is approached: $E = 3$ for $T_i = 318.15$ K, $E = 14$ for $T_i = 309.15$ K and $E = 16$ for $T_i = 308.15$ K. Therefore, the enstrophy is more than 5 times larger at 308.15 K than at 318.15 K, which clearly represents a substantial increase.

The distribution and the intensity of the convection cells directly affect the mass fraction field as revealed by Fig. 7 showing the vorticity field together with the isolines of $w_i - w$. The jet flow between contrarotative rolls is much weaker for $T_i = 318.15$ K allowing the development of a large mass fraction "plume" rising at the middle of the heated plate (Fig. 6). For $T_i = 308.15$ K, in contrast, the very intense convection flow restricts the diffusion of the solute mainly in the boundary layer along the plate. The mass fraction field obtained for $T_i = 309.15$ K is intermediate between those previously described (Fig. 6).

The effect of the proximity to the mixture critical point on heat and mass transfer was also evaluated on the mean Nusselt, Nu, and Sherwood, Sh, numbers on the heated plate, respectively defined by:

$$\mathrm{Nu} = -\frac{1}{L_{\mathrm{plate}}} \int_{\mathrm{plate}} \frac{H}{\lambda_i \Delta T} \lambda(T) \frac{\partial T}{\partial y} dx$$

and

$$\mathrm{Sh} = -\frac{1}{L_{\mathrm{plate}}} \int_{\mathrm{plate}} \frac{H}{(D_{21})_i \left(w(x,0,t) - w\left(x, \frac{H}{2}, t\right) \right)} D_{21} \frac{\partial w}{\partial y} dx$$

with $L_{\mathrm{plate}} = 8$ the dimensionless length of the heated plate. Results are reported in Table 5 for the three initial temperatures. We note a strong increase of both Nu and Sh as the critical temperature is approached (+ 86% for Nu, + 46% for Sh), which means that the neighborhood of the critical point favors heat and mass transfer from the heated plate. In [45], Lim et al. proposed several correlations of the Sherwood number for mass transfer at solid-fluid interfaces at supercritical conditions. For natural convection, the Sherwood number can be expressed as a function of the Schmidt $Sc = \mu_i / (\rho_{cm}(D_{21})_i)$ and Grashof $Gr = Ra/Pr$ numbers with the correlations:

$$\mathrm{Sh} = m_2 (Sc\ Gr)^{\frac{1}{4}} \text{for laminar convection} \tag{11}$$

$$\mathrm{Sh} = m_3 (Sc\ Gr)^{\frac{1}{3}} \text{for turbulent convection} \tag{12}$$

As shown in Fig. 8, the values of the mean Sherwood number that we obtained are consistent with Eq. (12) (with $m_3 = 0.182$) in the vicinity to the critical point. On the other hand, for the highest initial temperature, the Sherwood number is strongly underestimated by the correlation.

Table 5 Mean Nusselt and Sherwood numbers on the heated plate for the three initial temperatures

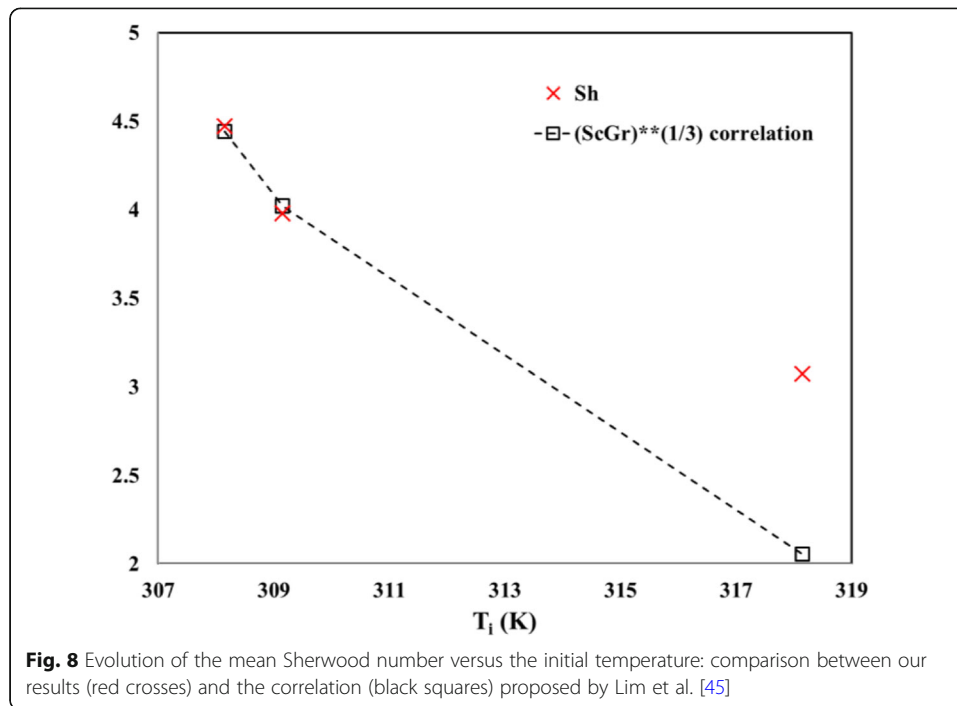| T_i (K)	Nu	Sh
308.15	1.9069	4.4723
309.15	1.8298	3.9796
318.15	1.0249	3.0723

Fig. 8 Evolution of the mean Sherwood number versus the initial temperature: comparison between our results (red crosses) and the correlation (black squares) proposed by Lim et al. [45]

Adsorption investigation in the vicinity of the lower critical endpoint

The adsorbed solute amount is greatly affected by the convection flow. Actually, Fig. 9a exhibits the relative mass fraction perturbation profile $(w_i - w)/w_i$ on the lower boundary for the three initial temperatures. Although the maximum amount adsorbed on the plate increases when moving away from the critical point, the profiles disclose that the adsorption of the solute is strongly inhomogeneous for T_i = 318.15 K, with a peak of adsorption in the middle of the plate, corresponding to the large mass fraction "plume" noted in Fig. 6. On the other hand, close to the critical point (T_i = 308.15 K), the peak in the central zone is less pronounced, leading to a more homogeneous adsorption of the solute and, therefore, a more homogeneous material in the framework of SFD processes for example.

The same tendency with respect to the distance to the critical point is observed on the temporal evolution of the relative mass fraction perturbation $(w_i - w)/w_i$ (Fig. 9b).
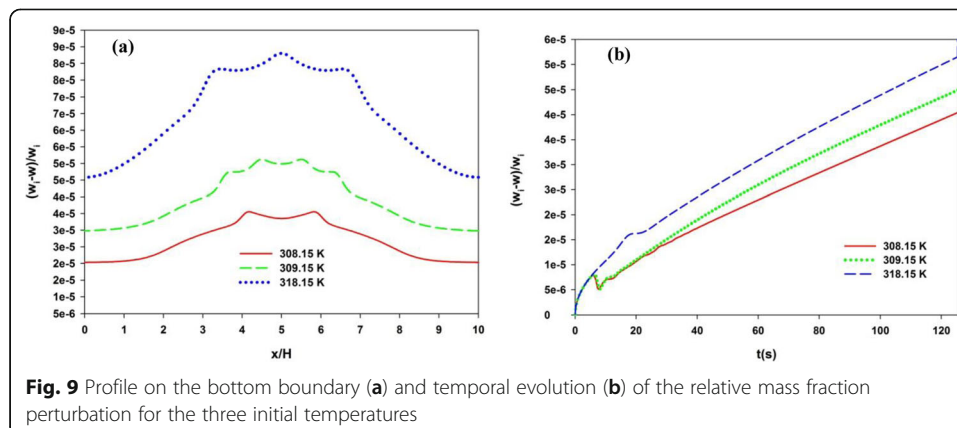
Fig. 9 Profile on the bottom boundary (**a**) and temporal evolution (**b**) of the relative mass fraction perturbation for the three initial temperatures

As already outlined in section 5.2, since Da ≪ 1, the reaction has not reached equilibrium although the mass fraction field in the cavity shows a stationary solution (Fig. 6), and, consequently, the mass fraction perturbation on the bottom plate keeps on increasing.

In order to quantify the effect of convection on the adsorbed amount, we have performed simulations in the same configuration with no gravity. The mean adsorbed amount of solute, defined by:

$$q_{mean} = \frac{1}{L_{plate}} \int_{plate} \frac{w_i - w}{w_i} dx$$

and obtained with and without gravity is reported in Table 6. First, it can be noted that, even in the absence of convection, the adsorbed amount of solute decreases when approaching the critical point (− 1.35% at T_i = 308.15 K compared to the value obtained at T_i = 318.15 K). This decrease is due to the increase near the critical point of the pressure rise induced by the piston effect (Fig. 5) and the negative value of the adsorption constant derivative with respect to pressure, leading to a decrease of the adsorption constant K_a (Eq. (9)). However, Table 6 also shows that this decrease of q_{mean} with the distance to the critical point is much larger in the presence of convection (− 15% at T_i = 308.15 K compared to the value obtained at T_i = 318.15 K). This stronger decrease is directly caused by the intense convection flow observed for the smallest initial temperature (Fig. 7). Indeed, the adsorbed amount also depends on the contact time of the solute with the adsorbent plate: the longer the solute is in contact with the adsorbent surface, the greater is the adsorbed amount.

In order to study the contact time of the solute molecules with the adsorbent plate, we represent in Fig. 10 the x profile of the vertical velocity v in the boundary layer along the bottom boundary for the three initial temperatures. These profiles are particularly interesting because they show that the smaller the temperature T_i is, the greater the vertical velocity v is and, consequently, the faster the solute molecules are removed from the vicinity of the adsorbent wall. Therefore, Fig. 10 clearly shows that the contact time of the solute decreases with the initial temperature. Moreover, the vertical velocity v for T_i = 308.15 K is 6 times larger than for T_i = 318.15 K. This large vertical velocity is directly related to the intense convection cells depicted by the vorticity field in Fig. 7. Therefore, we can conclude that, because of the increasing Rayleigh number near the critical point (induced by the divergence of the thermal expansion coefficient), the contact time of the solute with the adsorbent plate is strongly reduced and, consequently, the adsorbed amount of solute is decreased when the critical temperature is approached.

Table 6 Mean adsorbed amount of solute, q_{mean}, at t = 128s for the three initial conditions with (gravity) and without (g = 0) convection

T_i (K)	$(w_i − w)/w_i$	
	Gravity	**g = 0**
308.15	2.3981×10^{-5}	3.3332×10^{-5}
309.15	2.5267×10^{-5}	3.3385×10^{-5}
318.15	2.8329×10^{-5}	3.3787×10^{-5}

Fig. 10 Vertical velocity profiles for the three initial temperatures
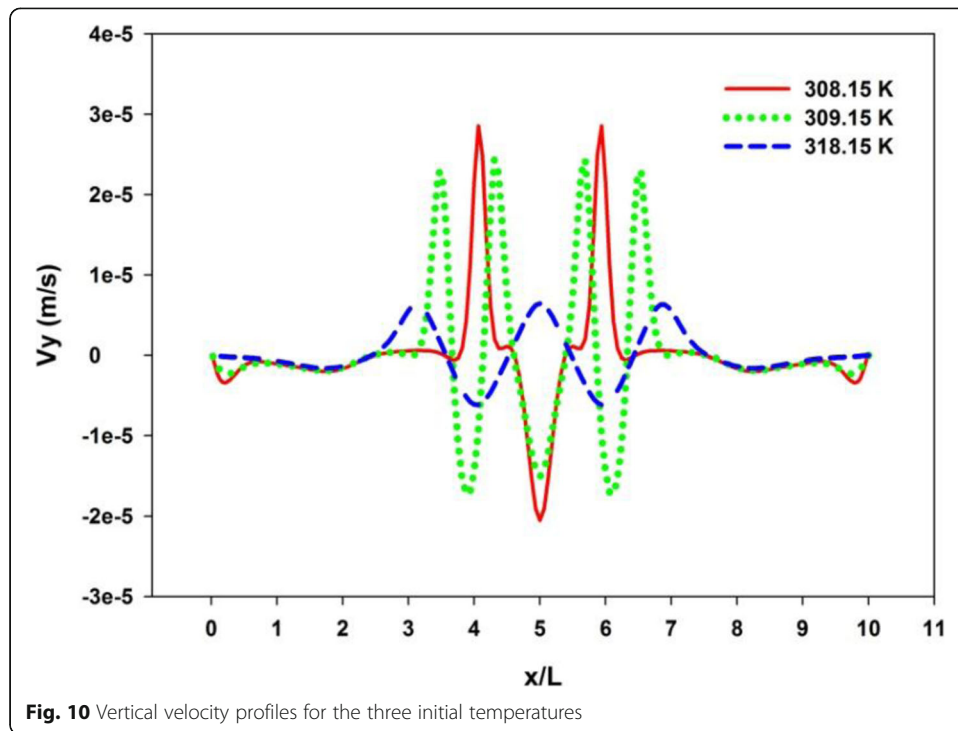
Conclusions

In this paper, we have presented a numerical study along with an exhaustive adsorption investigation in a binary dilute mixture model nearby the solvent's critical point. The results of our study revealed that, because of the divergence of the thermal expansion coefficient, the Rayleigh number strongly increases. As a consequence, an intense convection flow develops in the cavity when approaching the critical point, leading to a more homogeneous adsorption profile but reducing the adsorbed amount of solute. This decrease is due to the increase near the critical point of the pressure rise induced by the piston effect caused by the divergence of isothermal compressibility. Moving far from the critical point aims to reduce the fluid vertical velocity in the boundary layer along the wall enclosing the adsorbent plate, thereby increasing the solute contact time with the plate, leading to an increase of the adsorbed amount of solute. On the other hand, approaching the critical point allows a strong increase of the mass transfer at the adsorbent plate, deduced from the increase of the mean Sherwood number.

Nomenclature

P Pressure, Pa
T Temperature, K
V Velocity, m/s
Re Reynolds number
C_V Heat capacity, J kg^{-1} K^{-1}
Fr Froude number
Ra Rayleigh number
w Mass fraction
H Characteristic height, mm

L Cavity length, mm

Ma Mach number

PE Piston effect

Pr Prandtl number

Le Lewis number

R Perfect gas constant, J/kg K

Sh Sherwood number

t Time, s

u Velocity component in the x direction, m/s

v Velocity component in the y direction, m/s

x,y Cartesian axis directions, mm

D_{21} Binary mass diffusion coefficient, m^2/s

Greek symbols

ρ Density, kg m^{-3}

ε Dimensionless proximity to the critical point

μ Dynamic viscosity, Pa s

δt Dimensionless time step, s

β Thermal expansion coefficient, K^{-1}

γ Ratio of heat capacities

λ Thermal conductivity, W·m^{-1}·K^{-1}

ω Acentric factor

Subscripts

c Critical property

i Initial value

th Thermodynamic part

h Heat

0 Perfect gas property

(*) Dimensionless parameters

Availability of data and materials
All data generated or analyzed during this study are included in this published article and are available from the corresponding author.

Declarations

Competing interests
The authors declare that they have no competing interests.

Author details
[1]Laboratory of Theoretical Physics, University of Abou Bekr Belkaid, Tlemcen, Algeria. [2]Department of Physics, Faculty of Sciences, University of Abou Bekr Belkaid, Tlemcen, Algeria. [3]Department of Mathematics, Faculty of Sciences, University of Abou Bekr Belkaid, Tlemcen, Algeria. [4]Aix Marseille Univ, CNRS, Centrale Marseille, M2P2, Marseille, France.

References

1. Deshpande PB, Kumar GA, Kumar AR, Shavi GV, Karthik A, Reddy MS, Udupa N (2011) Supercritical fluid technology: concepts and pharmaceutical applications. PDA J Pharm Sci Technol 65:333–344. https://journal.pda.org/content/65/3/333. https://doi.org/10.5731/pdajpst.2011.00717
2. Pereira CG, Marques MO, Barreto AS, Siani AC, Fernandes EC, Meireles MA (2004) Extraction of indole alkaloids from Tabernaemontana catharinensis using supercritical CO_2+ethanol: an evaluation of the process variables and the raw material origin. J Supercritical Fluids 30(1):51–61. https://doi.org/10.1016/S0896-8446(03)00112-8
3. Peng J, Fan G, Wu Y (2005) Supercritical fluid extraction of aurentiamide acetate from Patrinia villosa Juss and subsequent isolation by silica gel and high-speed counter-current chromatography. J Chormatography A 1083(1-2):52–57. https://doi.org/10.1016/j.chroma.2005.05.097
4. Turner C, King JW, Mathiasson L (2001) Supercritical fluid extraction and chromatography for fat-soluble vitamin analysis. Journal of Chromatography 936(1-2):215–237. https://doi.org/10.1016/S0021-9673(01)01082-2
5. De Lucas A, De La Ossa EM, Rincon J, Blanco MA, Gracia I (2002) Supercritical fluid extraction of tocopherol concentrates from olive tree leaves. J Supercritical Fluids 22(3):221–228. https://doi.org/10.1016/S0896-8446(01)00132-2
6. Perrut M (2000) Supercritical fluid applications: industrial developments and economic issues. Ind Eng Chem Res 39(12):4531–4535. https://doi.org/10.1021/ie000211c
7. Brunner G (1994) Gas extraction: an introduction to fundamentals of supercritical fluids and the application to separation processes. Topics in Physical Chemistry, Vol. 4, Steinkopff-Verlag Heidelberg.
8. Chen L, Iwamoto Y (2017) Advanced applications of supercritical fluids in energy systems. Chen, Lin and Yuhiro Iwamoto. IGI Global. https://doi.org/10.4018/978-1-5225-2047-4
9. Kuo L, Zhenming X (2019) A review of current progress of supercritical fluid technologies for e-waste treatment. J Cleaner Prod 227:794–809. https://doi.org/10.1016/j.jclepro.2019.04.104
10. Eaton AD, Greenberg AE (1995) Standard methods for the examination of water and wastewater. American Public Health Association
11. Li Y, Wang S (2020) Supercritical water oxidation for environmentally friendly treatment of organic wastes. Advanced Supercritical Fluids Technologies, IntechOpen, London
12. Long C, Lu JD, Li A, Hu D, Liu F, Zhang Q (2008) Adsorption of naphthalene onto the carbon adsorbent from waste ion exchange resin: equilibrium and kinetic characteristics. J Hazard Mater 150(3):656–661. https://doi.org/10.1016/j.jhazmat.2007.05.015
13. Aisien FA, Amenaghawon AN, Adinkwuye AI (2014) Batch study, equilibrium and kinetics of adsorption of naphthalene using waste tyre rubber granules. J Xenobiot 4(1):2264. https://doi.org/10.4081/xeno.2014.2264
14. Shi Q, Li A, Zhu Z, Liu B (2013) Adsorption of naphthalene onto a high-surface-area carbon from waste ion exchange resin. J. Environ. Sci. 25(1):188–194. https://doi.org/10.1016/S1001-0742(12)60017-5
15. Ameur D, Raspo I (2013) Numerical simulation of the Poiseuille-Rayleigh-Bénard instability for a supercritical fluid in a mini-channel. Comput Thermal Sci 5(2):107–118. https://doi.org/10.1615/ComputThermalScien.2013006169
16. Erkey C (2009) Preparation of metallic supported nanoparticles and films using supercritical fluid deposition. J Supercritical Fluids 47(3):517–522. https://doi.org/10.1016/j.supflu.2008.10.019
17. Bozbag SE, Erkey C (2015) Supercritical deposition: current status and perspectives for the preparation of supported metal nanostructures. J Supercritical Fluids 96:298–312. https://doi.org/10.1016/j.supflu.2014.09.036
18. Raspo I, Meradji S, Zappoli B (2007) Heterogeneous reaction induced by the piston effect in supercritical binary mixtures. Chem Eng Sci 62(16):4182–4192. https://doi.org/. https://doi.org/10.1016/j.ces.2007.04.027
19. Hu Z-C, Zhang X-R (2019) Coupled extraction and crystal growth in supercritical solutions: Model and theory. J Supercritical Fluids 153:104578. https://doi.org/10.1016/j.supflu.2019.104578
20. Alonso A, Cantero FJ, Garcia J, Cocero MJ (2002) Scale-up for a process of supercritical extraction with adsorption of solute onto active carbon, Application to soil remediation. J Supercritical fluids 24(2):123–135. https://doi.org/10.1016/S0896-8446(02)00016-5
21. Kothandaraman S, Ahlert RC, Venkataramani ES, Andrews AT (1992) Supercritical extraction of polynuclear aromatic hydrocarbons from soil. Environ Prog Sustain. Energy 11(3):220–222. https://doi.org/10.1002/ep.670110317
22. Andrews AT, Ahlert RC, Kosson DS (1990) Supercritical fluid extraction of aromatic contaminants from a sandy loam soil. Environ Prog Sustain Energy 9(4):204–210. https://doi.org/10.1002/ep.670090413
23. Erkey CG, Orejuela M, Akgerman A (1993) Supercritical carbon dioxide extraction of organics from soil. Environ Sci Technol 27(6):1225–1231. https://doi.org/10.1021/es00043a025
24. Madras G, Erkey C, Akgerman A (1994) Supercritical extraction of organic contaminants from soil combined with adsorption onto activated carbon. J Environ Progress 13(1):45–50. https://doi.org/10.1002/ep.670130117
25. Madras G, Erkey C, Orejuela M, Akgerman A (1993) Supercritical fluid regeneration of activated carbon loaded with heavy molecular weight organics. Ind Eng Chem Res 32(6):1163–1168. https://doi.org/10.1021/ie00018a022
26. Srinivasan MP, Smith JM, McCoy BJ (1990) Supercritical fluid desorption from activated carbon. Chem Eng Sci 45(7):1985–1895. https://doi.org/10.1016/0009-2509(90)87064-Y

27. Macnaughton SJ, Foster NR (1995) Supercritical adsorption and desorption behavior of DDT on activated carbon using carbon dioxide. Ind Eng Chem Res 34(1):275–282. https://doi.org/10.1021/ie00040a029
28. Tan CS, Liou DC (1989) Supercritical regeneration of activated carbon loaded with benzene and toluene. Ind Eng Chem Res 28(8):1222–1226. https://doi.org/10.1021/ie00092a015
29. Tan CS, Liou DC (1988) Desorption of ethyl acetate from activated carbon by supercritical carbon dioxide. Ind Eng Chem Res 27(6):988–991. https://doi.org/10.1021/ie00078a017
30. Lucas S, Calvo MP, Palencia C, Cocero MJ (2004) Mathematical model of supercritical CO_2 adsorption on activated carbon: effect of operating conditions and adsorption scale-up. J Supercrit Fluids 32(1-3):193–201. https://doi.org/10.1016/j.supflu.2004.02.008
31. Jha SK, Madras G (2004) Modeling of adsorption equilibria in supercritical fluids. J Supercritical Fluids 32(1-3):161–166. https://doi.org/10.1016/j.supflu.2003.12.010
32. Wannassi M, Raspo I (2016) Numerical study of non-isothermal adsorption of Naphthalene in supercritical CO_2: behavior near critical point. J.Supercritical Fluids 117:203–218. https://doi.org/. https://doi.org/10.1016/j.supflu.2016.06.020
33. Ameur D, Smahi H, Dib J, Raspo I (2019) Numerical study of adsorption for fluids mixture near critical point in a micro-cavity. CFM 2019
34. Ameur D, Smahi H, Dib J, Raspo I (2018) Simulation of convective mass transfer in a near-critical binary mixture above an adsorbent boundary. 4th Conference on Energy, Materials, Applied Energetics and Pollution (ICEMAEP2018).
35. Smahi H, Ameur D, Dib J, Raspo I (2020) The confinement effect on a supercritical fluid mixture enclosed in a micro-cavity. In: Springer Proceedings in Energy. https://doi.org/10.1007/978-981-15-5444-5_14
36. Boukari H, Shaumeyer JN, Briggs ME, Gammon RW (1990) Critical speeding up in pure fluids. Physical Review A 41(4):2260–2263. https://doi.org/10.1103/PhysRevA.41.2260
37. Onuki A, Hao H, Ferrell RA (1990) Fast adiabatic equilibration in a single-component fluid near the liquid-vapor critical point. Physical Rev A 41(4):2256–2259. https://doi.org/10.1103/PhysRevA.41.2256
38. Zappoli B, Bailly D, Garrabos Y, Le Neindre B, Guenoun P, Beysens D (1990) Anomalous heat transport by the piston effect in supercritical fluids under zero gravity. Physical Rev A 41(4):2264–2267. https://doi.org/10.1103/PhysRevA.41.2264
39. Paolucci S (1982) Filtering of sound from the Navier-Stokes equations. Sandia National Laboratories, Livermore
40. Accary G, Raspo I, Bontoux P, Zappoli B (2005) An adaptation of the low Mach number approximation for supercritical fluid buoyant flows. C. R. Mecanique 331(5):397–404. https://doi.org/10.1016/j.crme.2005.03.004
41. Zappoli B (2003) Near-critical fluid hydrodynamics. C. R. Mecanique 331(10):713–726. https://doi.org/10.1016/j.crme.2003.05.001
42. Arai Y, Sako T, Takebayashi Y (2002) Supercritical Fluids: molecular interactions, physical properties and new applications. Springer, Berlin. https://doi.org/10.1007/978-3-642-56238-9
43. Wilke CR, Chang P (1955) Correlation of diffusion coefficients in dilute solutions. AIChE Journal 1(2):264–270. https://doi.org/10.1002/aic.690010222
44. Chang RF, Levelt Sengers JMH (1986) Behavior of dilute mixtures near the solvent's critical point. J Phys Chem 90(22):5921–5927. https://doi.org/10.1021/j100280a093
45. Lim G-B, Holder GD, Shah YT (1990) Mass transfer in gas-solid systems at supercritical conditions. J Supercrit Fluids 3(4):186–197. https://doi.org/10.1016/0896-8446(90)90022-E

Publisher's Note

Springer Nature remains neutral with regard to jurisdictional claims in published maps and institutional affiliations.